Laboratory demonstration of slow-rise to fast-acceleration of arched magnetic flux ropes

Bao N. Ha,[1]

Paul M. Bellan,[1]

B. N. Ha, Department of Applied Physics, California Institute of Technology, Pasadena, CA 91125, USA. (hab@caltech.edu)

P. M.Bellan, Department of Applied Physics, California Institute of Technology, Pasadena, CA 91125, USA. (pbellan@caltech.edu)

[1]Department of Applied Physics,

California Institute of Technology,

Pasadena, California, USA.

This article has been accepted for publication and undergone full peer review but has not been through the copyediting, typesetting, pagination and proofreading process, which may lead to differences between this version and the Version of Record. Please cite this article as doi: 10.1002/2016GL069744

We demonstrate the slow-rise to fast-acceleration of an arched plasma-filled magnetic flux rope. The flux rope expansion is inhibited by an externally-applied customizable strapping field. When the strapping field is not too strong and not too weak, expansion forces build up while the flux rope is in the strapping field region. When the flux rope moves to a critical height beyond the peak strapping field region, the plasma accelerates quickly corresponding to the observed slow-rise to fast-acceleration of solar eruptions. This behavior is in agreement with the predictions of the torus instability.

1. Introduction

Coronal mass ejections (CMEs) are eruptions of large plasma structures from the Sun. Their interaction with the Earth's atmosphere can destroy satellites, overwhelm power infrastructure, and harm astronauts. CMEs have a slow-rise phase followed by a rapid-acceleration phase [*Vrnak*, 2001], and the physical mechanisms behind coronal mass ejections are intensely debated [*Aulanier et al.*, 2010; *Chen*, 1989; *Roussev et al.*, 2003; *Moore et al.*, 2001; *Antiochos et al.*, 1999; *Fan and Gibson*, 2007]. Recent observation [*Zhang et al.*, 2012] and simulation [*Amari et al.*, 2014] proposed that a pre-existing magnetic flux rope structure, a 3D current channel with helical magnetic field, triggers the eruption through a loss of equilibrium mechanism. One such mechanism, the torus instability [*Kliem and Torok*, 2006; *Olmedo and Zhang*, 2010], occurs when a strapping field in the corona decays sharply as a function of height, allowing rapid acceleration of the flux rope when it rises above a critical height. Solar observations are unable to measure the magnetic field in the corona precisely and so solar models extrapolate the coronal magnetic field from photospheric magnetic measurements [*Amari et al.*, 2014; *Fan and Gibson*, 2007]. Unfortunately, extrapolation results differ [*Liu et al.*, 2011], and even the best non-linear force-free algorithms struggle to extrapolate the force-free corona magnetic field from the boundary measurements obtained from a "forced" photosphere [*Wiegelmann*, 2008]. In contrast, laboratory experiments of arched magnetic flux ropes [*Hansen and Bellan*, 2001; *Tenfelde et al.*, 2014; *Oz et al.*, 2011; *Tripathi and Gekelman*, 2010; *Stenson and Bellan*, 2012] can measure the magnetic field directly and permit systematic study of solar-relevant configurations by combining accessible diagnostics with high reproducibility.

We show in this Letter that expansion and strapping forces can be configured experimentally to produce different plasma loop behavior. The No Strapping field (NS) configuration provides a baseline and verifies that the hoop force dominates expansion dynamics [*Stenson and Bellan*, 2012], while application of a Large Strapping field (LS) completely inhibits loop expansion [*Hansen and Bellan*, 2001]. Our new result employs an Intermediate Strapping field (IS) to slow plasma expansion at early times allowing expansion forces to build up and contribute to the rapid acceleration of the plasma when it leaves the strapping field region. The sudden rapid acceleration also comes from the steep spatial decay of the strapping field, a feature that was not present in *Hansen and Bellan* [2001] which employed a uniform strapping field.

2. Experimental setup

The experimental setup is shown in Fig. 1. A pulsed, magnetic plasma gun consisting of anode, cathode, and bias coils is mounted at the end of a 1.5 m long, 0.92 m diameter vacuum chamber with 10^{-7} torr base pressure. The chamber is much larger than the plasma thus simulating a half-infinite space, and the chamber axis defines the z direction (height). The bias coils located behind the electrodes generate arched magnetic fields in the $y-z$ plane. The magnetic field is nominally 1.5 kG at the foot points and 250 G at the apex. Fast valves puff gas through the center of the bias coils into the vacuum chamber. High voltage applied to the electrodes by a 59 μF capacitor ionizes hydrogen gas to form an arched plasma of density $n \sim 10^{21}$ m^{-3}. The capacitor, which is typically charged to 2.5-5 kV, drives 30-70 kA current which flow in the y direction at the plasma loop apex. Additional inductance (L_{extra}) can be added to the intrinsic inductance of the

system ($L_{intrinsic}$) to slow down the current pulse. The plasma temperature T is estimated to be 2-4 eV corresponding to $\beta = 2\mu_0 n k_B T/B^2 \sim 0.2$, so magnetic forces are expected to dominate.

A 0.77 F capacitor bank powers two 7.6 cm diameter strapping field coils mounted 9.5 cm in front of the electrode. The strapping coils each have 11 turns and are placed in a coaxial configuration inside the chamber to produce a maximum 875 G strapping field in the x direction so that the $J_y \times B_x^{strap}$ force inhibits plasma loop expansion where J_y is the electric current density in the plasma loop. The NS, IS, and LS configurations correspond to 0 G, 250 G, and 500 G strapping field respectively.

Plasma dynamics are captured by two fast cameras and by magnetic probe clusters placed at 17.5 cm, 19.5 cm, 21.5 cm, and 25.5 cm in front of the electrodes along the chamber axis. One camera is a movie camera with line of sight perpendicular to the side view and provides the primary means of measuring plasma dynamics. The other camera faces the electrode from the opposite end of the vacuum chamber and provides disambiguation of projection effects. The probes provide localized, *in situ* measurements and can precisely time the plasma motion. The experiment is reproducible and shots can be repeated every two minutes. High resolution height (z) vs time data are obtained by repeating specific experiments with the same parameters many times and averaging. The strapping coils block viewing of the early evolution of the plasma, so quantitative imaging-based analysis is restricted to $z \geq 11$ cm. Information about the overall plasma structure is obtained by measuring the voltage and current across the electrodes and calculating the inductance of the plasma.

3. Results

Typical images of plasma expansion for the NS, IS, and LS configurations are shown in Figs. 2 (a), (b) and (c) where small white circles indicate the position of the plasma apex. The mean distances between these plasma apex positions and the electrodes are plotted as circles in Fig. 3; a mean distance is obtained by averaging shots with the same settings. These distance vs time measurements are smoothed and numerically differentiated to obtain velocity and acceleration, which are plotted in Fig. 4 as functions of both time and height.

Besides circles, Fig. 3 also has diamonds; these represent the average time for the plasma to travel to the magnetic probe clusters for NS and IS configurations. For the NS configuration this travel time is defined by when B_x reverses at a probe. This definition is chosen because B_x reverses polarity on the loop axis as seen in Fig. 2 (d). However, to give times consistent with the movie camera, the probe arrival time is defined to be when B_x peaks (Fig. 2 (e)) for the IS configuration. This different definition is because the strapping field tilts the flux rope axis, converting B_y and B_z components into B_x, making it difficult to determine the loop location by magnetic probe measurements alone.

To confirm that the NS configuration is dominated by the hoop force, we have verified that the time at which B_x polarity reverses scales in accordance with the predicted motion resulting from the hoop force. On defining $\alpha = \ln(8R/a) - 3/2 + 2\mu_0 P/B_\theta^2(a) + l_i/2$, the major radial force per unit length is

$$f_R = \frac{\mu_0 I^2}{4\pi R}\alpha \tag{1}$$

where I is the current, R and a are the loop major and minor radii, $B_\theta(a) = \mu_0 I/(2\pi a)$, P is the loop pressure, and l_i is the loop internal inductance [*Shafranov*, 1966]. Because the dependence of α on R is logarithmic, α is approximately constant with nominal value $\alpha \approx 2.5$. By assuming the current has a linear time dependence $I(t) = I_0 t/\tau$ where τ is the rise time and I_0 is the peak current, and then solving the equation of motion $m_i n \pi a^2 \ddot{R} = f_R$ where m_i is the ion mass and n is the plasma number density, Stenson and Bellan [2012] showed that the hoop force causes the major radius to expand as

$$R(t) = \frac{I_0 t^2}{2\pi a \tau} \left(\frac{\mu_0 \alpha}{2 m_i n} \right)^{1/2} \tag{2}$$

Equation 2 predicts constant loop acceleration (i.e., $\ddot{R} = const$) and that $t \propto (I_0/\tau)^{-1/2}$ for a given R. This t scaling prediction has been verified by varying τ and I_0 separately and then measuring the time for B_x reversal at a probe located at fixed R. Figure 5 plots the measured plasma travel time t to the B_x probe as a function of dI/dt, i.e., as a function of I_0/τ. The rise time τ at fixed I_0 is varied by changing the external inductance (shown by L_{extra} in Fig. 1) while adjusting the charging voltage of the 59 μF capacitor to maintain fixed I_0. The peak current I_0 is varied at fixed τ by varying the capacitor charging voltage. A log-log fit to the data (inset in Fig. 5) shows the measured time to reach the probe scales as $t_{probe} \propto (I_0/\tau)^{-\gamma}$ where $\gamma = 0.55$ for the B_x probe at $z = 17.5$ cm and $\gamma = 0.47 \pm 0.06$ using data from all four B_x probes. This near inverse square root dependence confirms that the dynamics of the NS configuration is dominated by the hoop force.

The application of the strapping field in the IS and LS configurations introduces the additional force $\mathbf{J}_{loop} \times \mathbf{B}_{strap}$ opposing the plasma loop major radius expansion. Figures 2 (b) and (c) show that the IS and LS configurations have more compact plasmas than the NS configuration (shown in Fig. 2 (a)), confirming that the strapping force opposes loop expansion. The detailed effect of the strapping field is determined by close examination of the NS, IS, and LS height, velocity, and acceleration data in Figs. 3 and 4. Figure 3 shows that at early times, the IS and the LS configurations (orange and red lines, respectively) have little initial expansion compared to the NS configuration (black line). Figure 3 also shows that the LS configuration is almost completely inhibited from expanding, and magnetic measurements do not detect the flux rope axis until $t > 15$ μs. This near complete confinement is further shown in Fig. 4, where it is seen that the LS velocity peaks at 10 μs when the driving current begins to decay (Fig. 6 (b) shows the time dependence of this current).

Our main result is given by the IS data, which demonstrates a slow initial rise of the plasma apex followed by a rapid acceleration. The nominal Alfvn velocity of the system is $v_A = B/\sqrt{\mu_0 \rho} \approx 40$ km/s and we define "fast" to be $v > 20$ km/s and "slow" to be $v < 13$ km/s. The sudden velocity increase (i.e., slow to fast transition) between 6 μs and 9 μs in Fig. 4 (a) and between 12 cm and 20 cm in Fig. 4 (b) corresponds to the plasma loop apex escaping the strong strapping field region, which is at $z = 9.5$ cm as indicated in Fig. 1 (side view). This escape coincides with an up to seven-fold increase in the acceleration of the plasma apex between 6 μs and 9 μs (Fig. 4 (c)) when compared to the NS case.

The increased acceleration is attributed to two effects: (i) the build-up of the hoop force when the plasma spends more time in the region of peak strapping field and (ii) the sharp spatial decay of the strapping field once the plasma loop has left the region of peak strapping field. The build-up of the hoop force comes from the $f \sim I^2/R$ scaling of major radial forces as given by Eq. 1; the hoop force builds up because of an increase in the percentage of capacitor current I_{cap} flowing through the bright plasma arch and a decreased radius of curvature R at the loop apex. In the NS configuration, as little as 10 percent of I_{cap} flows through the flux tube as the plasma expands [*Stenson and Bellan*, 2012]. In contrast, IS loops are more compact, brighter, and more contorted since the strapping field slows down the expansion of the plasma loop apex, R is approximately constant (i.e., is expanding much slower than the t^2 scaling of the NS configuration), yet total current I_{cap} is still increasing until $t = 7 - 8$ μs (see Fig. 6 (b)). Magnetic measurements suggest larger percentages of I_{cap} flow through more compact, brighter plasma loops and camera images suggest that IS loops have locally smaller curvature radius. This enhanced hoop force is balanced by the strapping field until the IS apex passes the critical height after which the rapid reduction in strapping force caused by the spatial decay of the strapping field leads to enhanced acceleration.

The steepness of the strapping field decay is represented by the magnetic decay index $n = -(z/B_x)(dB_x/dz)$. The value of n varies with axial position z (up-sloping dashed line in Fig. 1 side view). When n exceeds a critical value n_{cr}, the plasma loop is predicted to undergo torus instability [*Kliem and Torok*, 2006], i.e., the restoring force associated with the strapping field decays more than the hoop force. The value of n_{cr} has been

predicted to range between $1-2$ [*Kliem and Torok*, 2006; *Dmoulin and Aulanier*, 2010; *Fan and Gibson*, 2007; *Schrijver et al.*, 2008], depending on geometry and boundary conditions. As a guideline, we use $n_{cr} = 3/2 - 1/(4c_0)$ from *Kliem and Torok* [2006] where $c_0 = L/\mu_0 R$ is the same as α in Eq. 2. While there are concerns [*Chen*, 2007] about the lack of footpoints in *Kliem and Torok* [2006], simulations including footpoints [*Olmedo and Zhang*, 2010] suggest that the essential physics of *Kliem and Torok* [2006] should apply. For our experiment, we calculate $\alpha \approx 2.5$ at plasma formation, resulting in $n_{cr} \approx 1.4$ which is plotted as the dotted horizontal line in Fig. 1 side view. The torus instability is expected approximately when the plasma loop moves to the right of the intersection of the dashed up-sloping line and this dotted horizontal line.

The load inductance is a measure of the entire plasma structure and is expected to scale as: $L \sim \mu_0 R\alpha$ where $\alpha \approx 2.5$. We calculate the time evolution of the inductance by neglecting resistance and using $V = L(dI/dt) + I(dL/dt)$ where V is the voltage measured across the plasma footpoints and I is the current through the plasma (Fig. 6 (a) and (b)). This equation can be discretized for a time step Δt:

$$L_{j+1} = L_{j-1} + \frac{2V_j \Delta t}{I_j} - \frac{L_j}{I_j}\left(I_{j+1} - I_{j-1}\right). \tag{3}$$

To obtain an initial condition, we assume $L_0 = V_0/(dI/dt)_0$ since I is very small at early times. Furthermore, since plasma expansion is minimal at early times, we assume $L_{-1} = L_0$. Resistance is non-negligible at breakdown and the plasma is cold slightly after breakdown, so we assume Eq. 3 is valid for $t > 2$ μs. The solutions are then valid for the time interval of interest: 2 $\mu s < t < 14$ μs; I is finite during this interval so Eq. 3 is well behaved.

Figure 6 (c) shows the inductance calculated using Eq. 3 for NS, IS, LS configurations; each plot is constructed using the average of ≈ 30 measurements for current and voltage. Figure 6 (c) shows that stronger strapping field leads to a smaller initial inductance and a smaller inductance growth. By using $R \sim L/(\mu_0 \alpha)$ at 2 μs, the calculated major radii are 3.2 cm, 2.2 cm, and 2.0 cm for NS, IS, and LS configurations respectively. Similar calculations at the time of peak current ($t = 8.5$ μs) yield $R \sim 6.2$ cm, 5 cm, and 3.3 cm respectively. The calculations are within a factor of 2 of the measured [effective] radii at the loop apex.

4. Discussion

Our observations demonstrate that torus instability is a means by which magnetic flux ropes may change from slow-rise to fast-acceleration. *Kliem and Torok* [2006] assumes a hypothetical perturbation without specifying the nature of said perturbation. Our results suggests that "increasing current" is an embodiment of this perturbation and the time dependence of the current may be important; if the current rises too quickly, the loop develops more momentum than for a slow-rising current so a stronger strapping field is required to oppose the expansion. We find the most dramatic acceleration for IS-like configurations occurs when we tailor the current pulse to peak as the plasma enters the region of steeply decaying strapping field.

Since Lorentz forces do not have an intrinsic length scale, it is reasonable to expect that our results should scale to solar loops provided that solar stratification is taken into account. The β of the solar atmosphere varies between the photosphere and the outer corona [*Aschwanden*, 2005]. Our results should apply in the lower corona, where $\beta \ll 1$

and the magnetic energy density is 800 times the gravitational energy density [*Forbes*, 2000]. The NS configuration represents a flux rope erupting as a consequence of energy and magnetic flux injected during the eruption (no energy storage) but this configuration is unlikely in the corona because the required injection rates would be excessive [*Schuck*, 2010]. The LS configuration corresponds to failed eruptions [*Ji et al.*, 2003], i.e., the solar filament erupts from the solar surface but fails to escape the solar atmosphere. The IS configuration, our new result, provides the first experimental demonstration of the slow-rise to fast-acceleration; this configuration corresponds to the majority of CMEs [*Vrnak*, 2001].

Acknowledgments. We thank Dave Felt for his technical assistance. This material is based upon work supported by the National Science Foundation under Award Number 1059519, by the Air Force Office of Scientific Research under Award Number FA9550-11-1-0184, and by the U.S. Department of Energy Office of Science, Office of Fusion Energy Sciences under Award Numbers DE-FG02-04ER54755 and DE-SC0010471. Experimental data available upon request.

References

Amari, T., A. Canou, and J.-J. Aly, Characterizing and predicting the magnetic environment leading to solar eruptions, *Nature*, *514*(7523), 465–469, doi:10.1038/nature13815, 2014.

Antiochos, S., C. DeVore, and J. Klimchuk, A model for solar coronal mass ejections, *The Astrophysical Journal*, *510*, 485–493, 1999.

Aschwanden, M., *Physics of the Solar Corona*, Springer Praxis Books, Springer Berlin Heidelberg, 2005.

Aulanier, G., T. Trk, P. Dmoulin, and E. E. DeLuca, Formation of Torus-Unstable Flux Ropes and Electric Currents in Erupting Sigmoids, *The Astrophysical Journal*, *708*(1), 314–333, doi:10.1088/0004-637X/708/1/314, 2010.

Chen, J., Effects of toroidal forces in current loops embedded in a background plasma, *The Astrophysical Journal*, *338*, 453–453, 1989.

Chen, J., Comment on "Torus Instability", *Physical Review Letters*, *99*(9), 099,501, doi:10.1103/PhysRevLett.99.099501, 2007.

Dmoulin, P., and G. Aulanier, Criteria for Flux Rope Eruption: Non-Equilibrium Versus Torus Instability, *The Astrophysical Journal*, *718*(2), 1388–1399, doi:10.1088/0004-637X/718/2/1388, 2010.

Fan, Y., and S. Gibson, Onset of coronal mass ejections due to loss of confinement of coronal flux ropes, *The Astrophysical Journal*, *668*(2), 1232–1245, doi:10.1086/521335, 2007.

Forbes, T. G., A review on the genesis of coronal mass ejections, *Journal of Geophysical Research*, *105*(A10), 23,153, doi:10.1029/2000JA000005, 2000.

Hansen, J. F., and P. M. P. M. Bellan, Experimental demonstration of how strapping fields can inhibit solar prominence eruptions, *The Astrophysical Journal*, *563*(563), 183–186, doi:10.1086/338736, 2001.

Ji, H., H. Wang, E. J. Schmahl, Y.-J. Moon, and Y. Jiang, Observations of the Failed Eruption of a Filament, *The Astrophysical Journal Letters*, *595*(2), L135, 2003.

Kliem, B., and T. Torok, Torus Instability, *Physical Review Letters*, *96*(25), 255,002–255,002, doi:10.1103/PhysRevLett.96.255002, 2006.

Liu, S., H. Q. Zhang, and J. T. Su, Comparison of Nonlinear Force-Free Field and Potential Field in the Quiet Sun, *Solar Physics*, *270*(1), 89–107, doi:10.1007/s11207-011-9741-6, 2011.

Moore, R., A. Sterling, H. Hudson, and J. Lemen, Onset of the magnetic explosion in solar flares and coronal mass ejections, *The Astrophysical Journal*, *552*, 833–848, 2001.

Olmedo, O., and J. Zhang, Partial Torus Instability, *The Astrophysical Journal*, *718*(1), 433–440, doi:10.1088/0004-637X/718/1/433, 2010.

Oz, E., C. E. Myers, M. Yamada, H. Ji, R. M. Kulsrud, and J. Xie, Experimental verification of the Kruskal-Shafranov stability limit in line-tied partial-toroidal plasmas, *Physics of Plasmas (1994-present)*, *18*(10), 102,107, doi:10.1063/1.3647567, 2011.

Roussev, I. I., T. G. Forbes, T. I. Gombosi, I. V. Sokolov, D. L. DeZeeuw, and J. Birn, A Three-dimensional Flux Rope Model for Coronal Mass Ejections Based on a Loss of Equilibrium, *The Astrophysical Journal Letters*, *588*(1), L45, 2003.

Schrijver, C. J., C. Elmore, B. Kliem, T. Torok, and A. M. Title, Observations and modeling of the early acceleration phase of erupting filaments involved in coronal mass ejections, *The Astrophysical Journal*, (2001), 586–595, 2008.

Schuck, P. W., The photospheric energy and helicity budgets of the flux-injection hypothesis, *The Astrophysical Journal*, *714*(1), 68–88, doi:10.1088/0004-637X/714/1/68,

2010.

Shafranov, V. D., Plasma Equilibrium in a Magnetic Field, *Reviews of Plasma Physics*, *2*, 103, 1966.

Stenson, E. V., and P. M. Bellan, Magnetically Driven Flows in Arched Plasma Structures, *Physical Review Letters*, *109*(7), 075,001–075,001, doi: 10.1103/PhysRevLett.109.075001, 2012.

Tenfelde, J., F. Mackel, S. Ridder, T. Tacke, P. Kempkes, and H. Soltwisch, Apex expansion of magnetized plasma loops in a laboratory experiment, *Plasma Physics and Controlled Fusion*, *56*(5), 055,011, doi:10.1088/0741-3335/56/5/055011, 2014.

Tripathi, S. K. P., and W. Gekelman, Laboratory Simulation of Arched Magnetic Flux Rope Eruptions in the Solar Atmosphere, *Physical Review Letters*, *105*(7), 1–4, doi: 10.1103/PhysRevLett.105.075005, 2010.

Vrnak, B., Dynamics of solar coronal eruptions, *Journal of Geophysical Research: Space Physics*, *106*(A11), 25,249–25,259, doi:10.1029/2000JA004007, 2001.

Wiegelmann, T., Nonlinear force-free modeling of the solar coronal magnetic field, *Journal of Geophysical Research*, *113*(A3), A03S02–A03S02, doi:10.1029/2007JA012432, 2008.

Zhang, J., X. Cheng, and M.-d. Ding, Observation of an evolving magnetic flux rope before and during a solar eruption., *Nature communications*, *3*, 747–747, doi: 10.1038/ncomms1753, 2012.

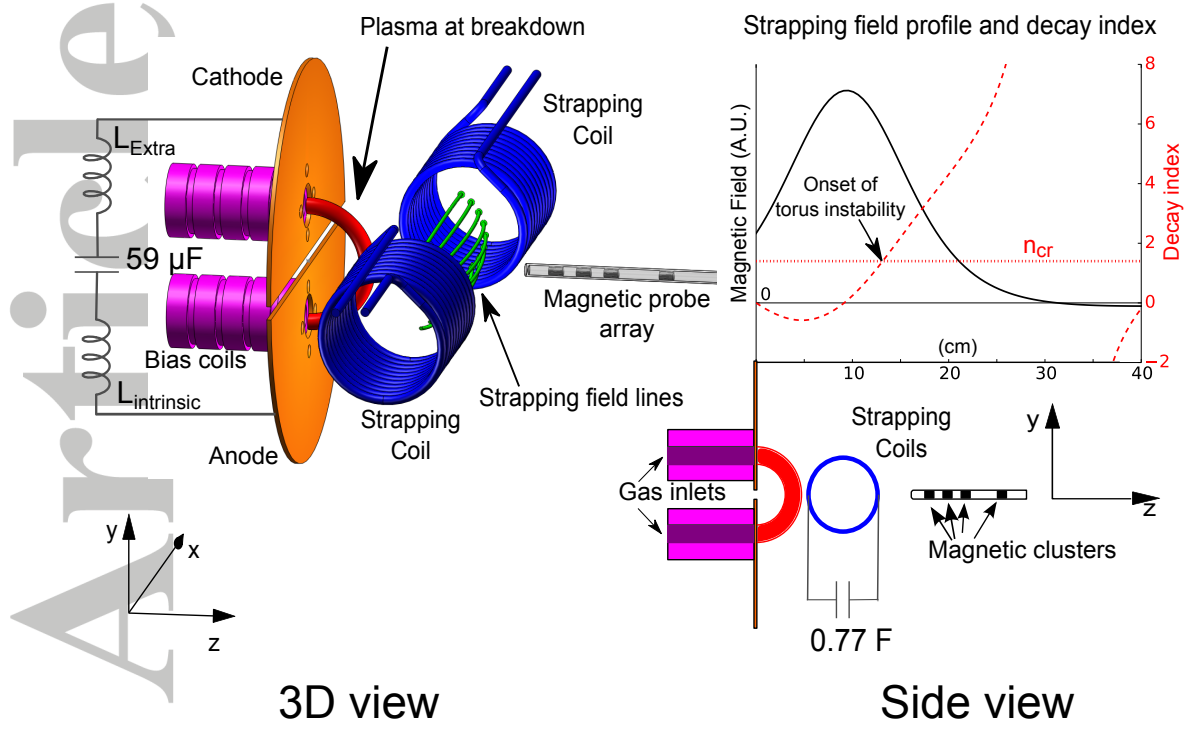

Figure 1. (color online) Schematic representation of experiment. The cathode and anode define the $x - y$ plane of the coordinate system, with the gap separating cathode from anode defining the origin. The bias coils (purple) generate arched magnetic fields similar to a horseshoe magnet. Independently powered coils (blue) produce strapping field (green arrows) and the plot in the upper part of the side view shows how the strapping field magnitude varies along the z axis. In the plot, the up-sloping dashed line (red) shows the calculated decay index of the strapping field and the horizontal dotted line (red) shows the calculated instability threshold. Additional inductance (L_{extra}) can be added to the intrinsic inductance of the system ($L_{intrinsic}$) to slow down the current pulse. The plasma (red) starts small but grows to many times its original size as it expands into the vacuum chamber.

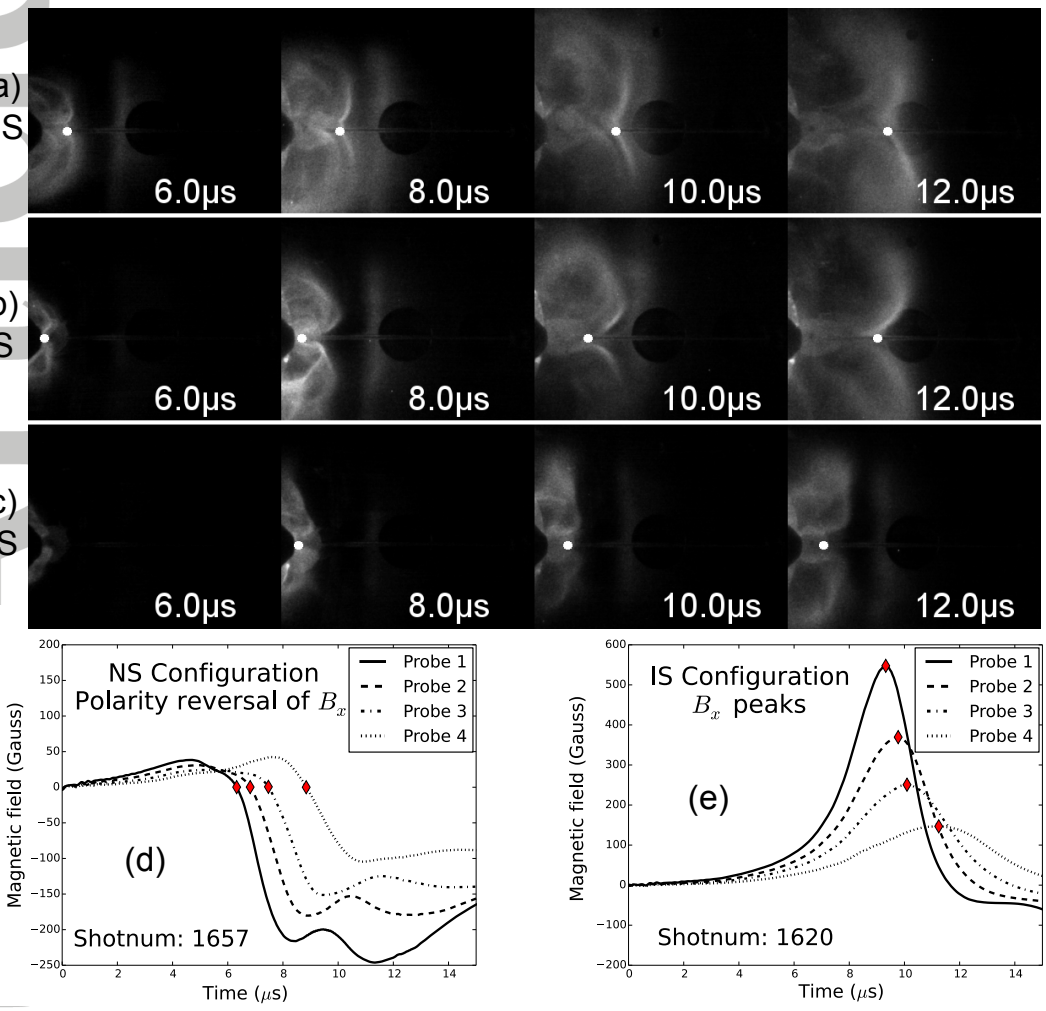

Figure 2. Imaging and magnetic diagnostics. The dots in (a), (b), and (c) represent the location of the plasma apex and is determined by looking at intensity slices along the z-axis and selecting the local intensity maximum. (d) and (e) show B_x component of the magnetic trace across all four magnetic probe clusters. The diamonds correspond to the bright (high density) leading edges from the camera images.

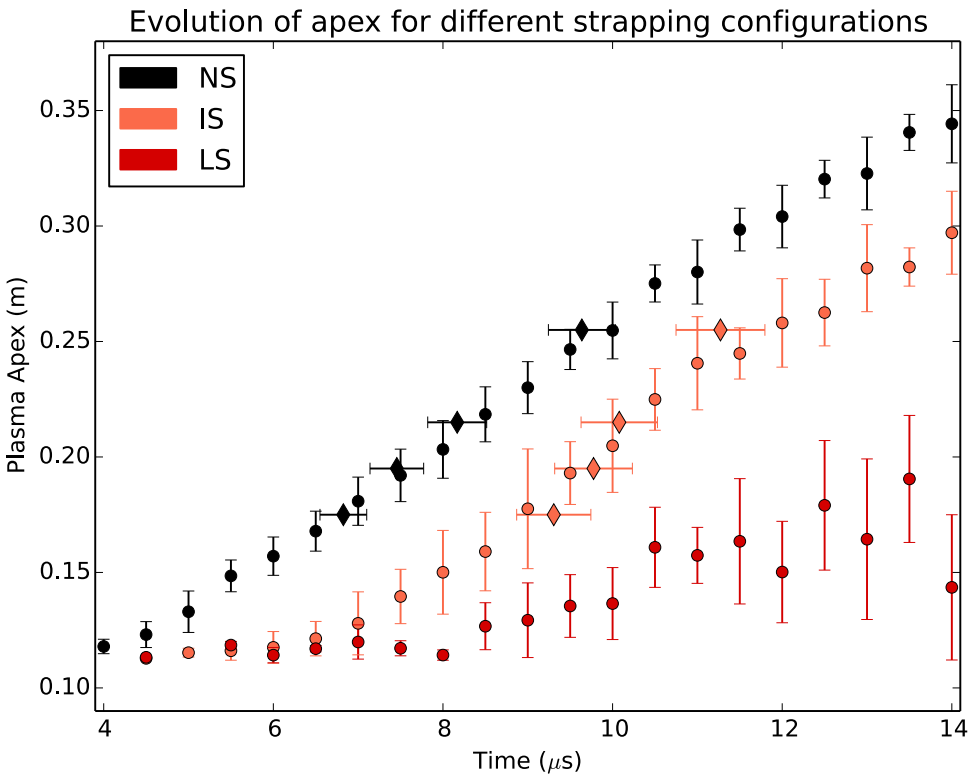

Figure 3. (color online) Height (z) vs time plot of different strapping configurations. The circles represent data obtained from imaging the plasma. The diamonds represent plasma position determined by the magnetic probes. In the LS configuration, the plasma does not reach the magnetic probe in the 14 μs time interval.

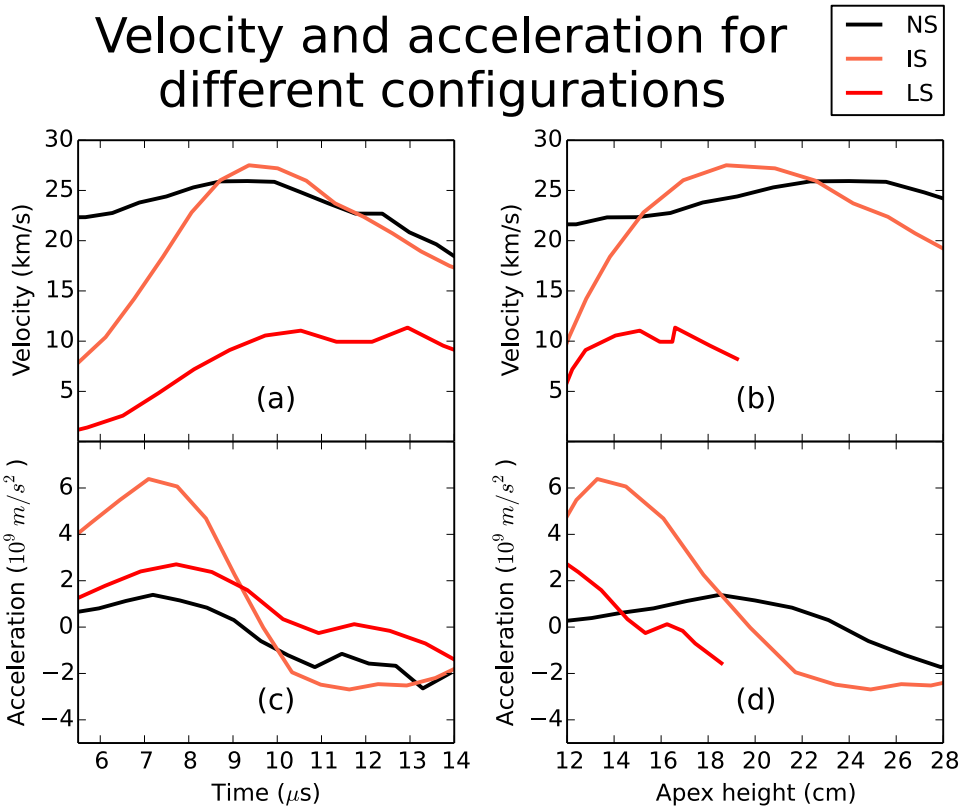

Figure 4. (color online) (a) Velocity obtained by smoothing the distance vs time measurements and then taking the numerical derivative for the three strapping configurations shown in Fig. 3. (b) Velocity as a function of apex height (z). (c) and (d) show acceleration obtained by smoothing the velocity and applying a numerical derivative.

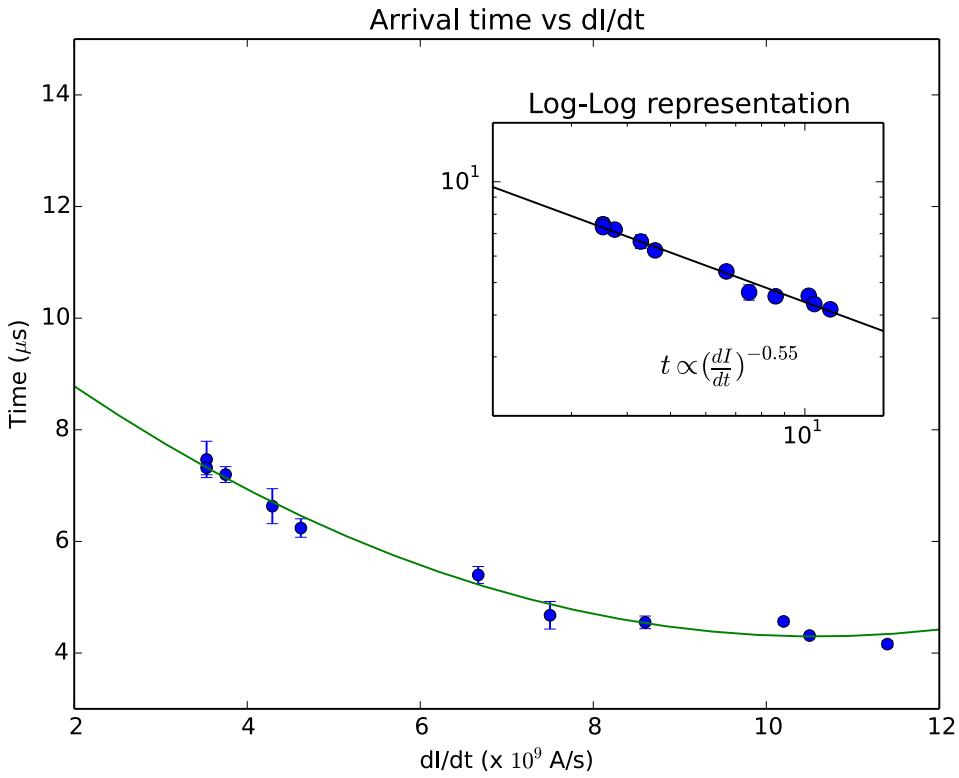

Figure 5. Time for the plasma to travel to the first magnetic probe cluster. dI/dt is varied by changing the peak current I_0 and the rise time of the current pulse τ independently. The inset is a log-log representation of the data and shows the relation $t_{probe} \propto (I_0/\tau)^{-0.55}$.

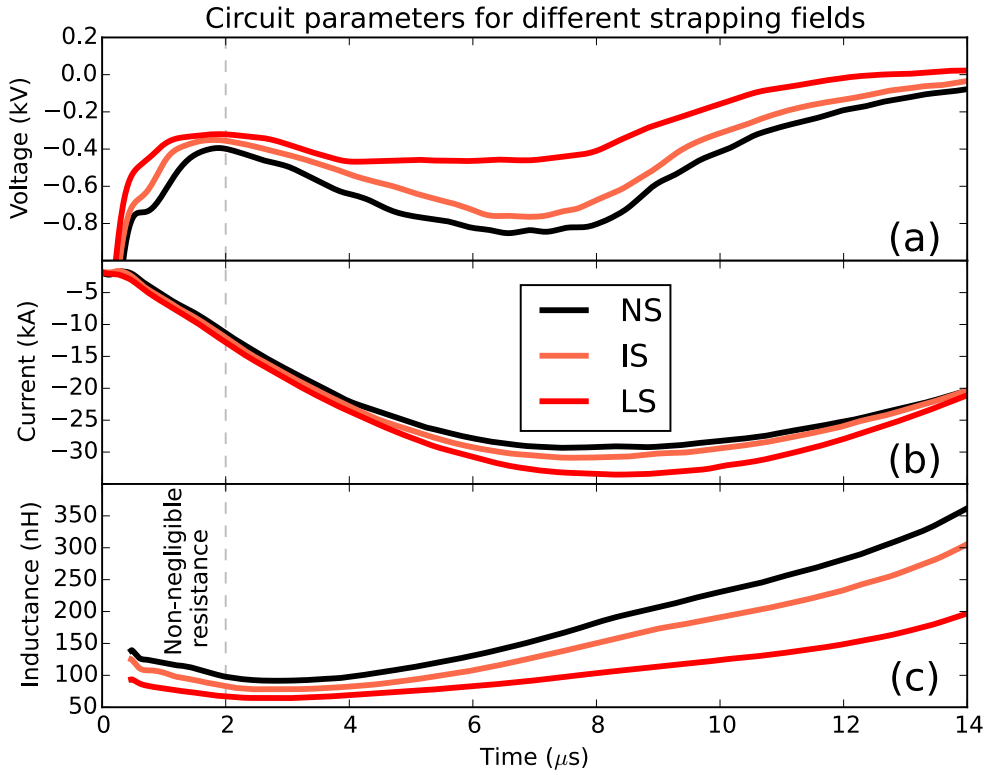

Figure 6. (color online) (a) Measured voltage and (b) measured system current I_{cap} for different strapping field configurations. (c) Calculated inductance vs time from voltage and current measurements using Eq. 3.